CORA Cork Open Research Archive
Cartlann Taighde Oscailte Chorcaí

Title	Strategies for passivating microneedle-based sensors: development, characterization and comparison
Authors	Bocchino, Andrea;Rodrigues Teixeira, Sofia;Barry, Fiona;Thatte, Chinmay;Ryan, Adam;Rahman, Fahima;Hu, Yuan;Iadanza, Simone;Galvin, Paul;Kurzhals, Steffen;Melnik, Eva;Mutinati, Giorgio C.;O'Mahony, Conor
Publication date	2025
Original Citation	Bocchino, A., Teixeira, S. R., Barry, F., Thatte, C., Ryan, A., Rahman, F., Hu, Y., Iadanza, S., Galvin, P., Kurzhals, S. and Melnik, E. (2025) 'Strategies for passivating microneedle-based sensors: development, characterization and comparison', Sensors and Actuators Reports, 9, p.100328. DOI: 10.1016/j.snr.2025.100328
Type of publication	Article (peer reviewed)
Link to publisher's version	10.1016/j.snr.2025.100328
Rights	© 2025, the Author(s). Published by Elsevier B.V. This is an open access article under the CC BY license (http://creativecommons.org/licenses/by/4.0/) - https://creativecommons.org/licenses/by/4.0/
Download date	2026-11-16 09:59:53
Item downloaded from	https://hdl.handle.net/10468/17365

UCC
University College Cork, Ireland
Coláiste na hOllscoile Corcaigh

Sensors and Actuators Reports 9 (2025) 100328



Contents lists available at ScienceDirect

Sensors and Actuators Reports

journal homepage: www.sciencedirect.com/journal/sensors-and-actuators-reports



Strategies for passivating microneedle-based sensors: development, characterization and comparison

Andrea Bocchino [a,*], Sofia Rodrigues Teixeira [a], Fiona Barry [a], Chinmay Thatte [a], Adam Ryan [a], Fahima Rahman [a], Yuan Hu [a], Simone Iadanza [a,b,c], Paul Galvin [a], Steffen Kurzhals [d], Eva Melnik [d], Giorgio C. Mutinati [d], Conor O'Mahony [a,*]

[a] Tyndall National Institute, University College Cork, Ireland
[b] Laboratory of Nano and Quantum Technologies, Paul Scherrer Institute, Forschungstrasse 111, 5232 Villigen, Switzerland
[c] Laboratory of Integrated Nanoscale Photonics and Optoelectronics, Ecole Polytechnique Federale de Lausanne, Route Cantonale, 1015 Lausanne, Switzerland
[d] AIT Austrian Institute of Technology GmbH, Center for Health and Bioresources, Molecular Diagnostics, Vienna, Austria

ARTICLE INFO

Keywords:
Microneedles
Passivation
Sensors
Electrochemistry

ABSTRACT

Microneedles (MNs) are sharp, pillar-like structures shorter than 1 mm. They can painlessly pierce the *stratum corneum* (SC), the outermost layer of the skin, and interface with the underlying dermal interstitial fluid, rich in biomarkers. Due to these properties, MNs have been widely investigated for several diagnostic applications. In particular, MN-based biosensors could enable the development of the new generation of minimally invasive continuous monitoring systems. To become a biosensor, the body or the tip of the needles must be functionalized. In addition, the area surrounding the MNs is usually passivated to prevent substrate interferences. Although passivation layers are widely used, there is a lack of characterization of such layers. This work aims at filling this gap, by developing, characterizing, and comparing six different passivation techniques. These include the application of polymethyl methacrylate (PMMA), Epotek 353ND, silicon oxide (SiO_2), parylene, varnish and an adhesive film to microneedle arrays. The performance of each method was then assessed using electrochemical measurements, optical and SEM imaging, and contact angle analysis.

Significant variability was observed across the various methods and materials. When assessed in terms of the electrochemically active area available after passivation, the tape and parylene were the most promising layers, while varnish and epoxy were the worst performing materials. The PMMA performed better than the other liquid passivations, but still requires refinement due to the high degree of unwanted coverage of the needles. Finally, the SiO_2 layer seemed to be a viable option, but also remains in need of additional optimization.

1. Introduction

Interstitial fluid (ISF) is an extracellular fluid that surrounds blood vessels and cells, and that comprises 15–25 % of body weight [1]. This fluid filters from the capillaries and is then removed through the lymphatic system [2]. Thanks to this circulatory mechanism, ISF is rich in biomarkers, ions and compounds. Their concentrations are in near equilibrium with those found in blood. For these reasons, together with the high amount of ISF present in the body, interstitial fluid has been widely investigated as a means of disease detection, healthcare diagnostics and monitoring of athletic performances [3–5].

A number of methods may be used to sample ISF, including the use of suction blisters, biopsies, reverse iontophoresis, microdialysis or implantable sensors [6]. However, each of these techniques has limitations such as the need for minor surgery, clinical expertise, and patient discomfort.

An emerging alternative involves the use of microneedle-based devices [7] – arrays of short, sharp structures that painlessly penetrate the skins outermost *stratum corneum* layer. They are too short to stimulate the underlying nerve endings or strike the capillary network that lies

* Corresponding authors.
E-mail addresses: Andrea.bocchino@tyndall.ie (A. Bocchino), Sofia.teixeira@tyndall.ie (S. Rodrigues Teixeira), Fiona-barry@hotmail.com (F. Barry), Chinmay.thatte@tyndall.ie (C. Thatte), Adamryan.info@gmail.com (A. Ryan), Fahimaway7@gmail.com (F. Rahman), Yuan.hu@tyndall.ie (Y. Hu), Simone.iadanza@psi.ch (S. Iadanza), Paul.galvin@tyndall.ie (P. Galvin), Steffen.kurzhals@ait.ac.at (S. Kurzhals), Eva.melnik@ait.ac.at (E. Melnik), Giorgio.mutinati@ait.ac.at (G.C. Mutinati), Conor.omahony@tyndall.ie (C. O'Mahony).

https://doi.org/10.1016/j.snr.2025.100328
Received 2 January 2025; Received in revised form 14 April 2025; Accepted 16 April 2025
2666-0539/© 2025 The Author(s). Published by Elsevier B.V. This is an open access article under the CC BY license (http://creativecommons.org/licenses/by/4.0/).

deeper in the epidermis [8,9].

Microneedles were initially developed for use in drug and vaccine delivery [10], but have also been demonstrated for ISF sampling and analysis [7]. Since microneedles provide a direct interface with ISF [11], hollow MNs can be used to withdraw fluid for out-of-the-body analysis [12]. Electrochemically modified solid needles may also be applied to the skin for continuous monitoring [13]. Typical examples of MN-based sensor applications include detection of biomarkers such as lactate [14] and glucose [15], pH measurement [16], or analysis of different electrolytes [17].

To act as an ISF sensor, the needles need to be electrically conductive and are usually metallised using different techniques, such as thermal evaporation, e-beam deposition or electroplating. Target-specific chemistries are then bonded to the structures. However, in many cases the substrate is metallised along with the needles themselves. Therefore, the substrate must be passivated to block any functionalisation in those areas. Failure to do so may lead to unwanted responses from interferents on the skin outside of the SC. This substrate passivation limits reactions to those which take place on the body of the needle and, therefore, improves selectivity and sensitivity to the target analyte.

An ideal passivation layer should firstly have a high and uniform electrical resistance, avoiding any type of undesired interference between substrate metallisation and electrochemical layers. Secondly, the layer should be relatively thin in comparison to the needle height, as the material thickness obviously reduces the height available for skin penetration.

To be as effective as possible, the layer should entirely cover the substrate around the MNs. Moreover, after application, MNs are usually not fully embedded into the skin [18]. In this case, the lower region of the needles may then come into contact with other external media, such as sweat. These media could potentially influence the readout of the sensor. Therefore, an ideal passivation should also cover this lower region. Here, the passivation should be conformal to the MNs themselves, and should avoid reducing their usable height. It should also be precisely controllable, i.e. capable of being accurately deposited and patterned or etched, to leave the desired portion of the MNs available for functionalization. To be used *in-vivo*, the passivation material should be biocompatible with standards such as ISO 10,993–5 and −10 for cytotoxicity and skin sensitization. Finally, it should also be compatible with mass manufacturing techniques.

Fig. 1 depicts two different passivation layers: one is representation of an 'ideal' passivation layer (A), while the second presents several issues (B). Firstly, the thickness of the ideal passivation layer (T) is much smaller than the height of the MNs (H). The passivation also covers the lower region (LR) of the needles in a conformal fashion, limiting the reduction in usable height to the thickness of the layer (T). In contrast, the second, suboptimal example is much thicker (T') and not conformal to the needles, strongly reducing the height available for skin penetration (H-T').

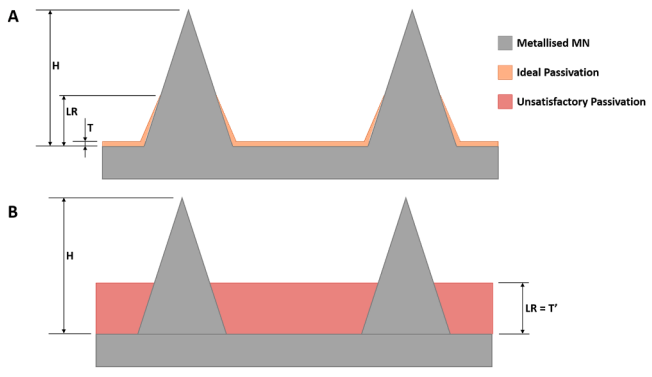


Fig. 1. Visual representation of an ideal (A) and an unsatisfactory (B) passivation layer.

Table 1 reports examples of metallised and passivated MNs devices used for diagnostic applications. Different passivation techniques include spin-coating [19–21], oxide formation [22], manual application of varnish or enamel [23–25] and chemical vapour deposition (CVD) [26,27].

Although passivation layers are increasingly used for ISF diagnostics, relatively little data related to the characterization of such layers has been reported. We have previously developed a platform for the rapid prototyping of microneedle-based devices – a process that includes application of passivation layers for diagnostic purposes [31]. Preliminary data relating to passivation materials and techniques have also been reported in a previous work [32]. In this paper, we provide a more extensive analysis of existing and new passivation layers, including varnish, parylene, silicon oxide (SiO_2), polymers (PMMA and Epotek 353ND, a USP class VI epoxy) and a medical grade adhesive film (ARcare 7759). The processes used to apply these coatings are also reviewed to provide additional insight regarding advantages and disadvantages of the different techniques and materials. Visual and electrochemical analyses were used to compare the layers in terms of reproducibility, uniformity and electrochemically active area. It is intended that this screening work will form a basis from which future research will continue optimizing the most promising passivation methods. This research should be focussed on maximising performance, scalability, and reproducibility.

Significant variability was observed across the various methods and materials, highlighting the need for further research and process development in this area. When assessed in terms of the electrochemically active area available after passivation, the tape and parylene were the most promising layers, while varnish, epoxy and PMMA were the worst performing materials. Finally, SiO_2 seemed to be a viable option, but it remains in need of additional optimization.

2. Materials and methods

2.1. Microneedle array production

A 100 mm diameter silicon MN wafer was produced through wet KOH etching [33] and glued (NOA68 from Norland Products NJ, USA) to a glass petri dish to form a front side master template. The needles were in the shape of ultra-sharp, 500 μm tall octagonal pyramids with a tip-to-tip distance of 1750 μm. The octagonal shape of the needles is determined by the orientation of the crystalline planes, and their interaction with the KOH etchant and the surface masks [33]. The height and pitch were selected based on prior experience and in-vivo experimental work, such as [34], where the 500 μm tall needles showed good skin penetration, biomechanical robustness and quick skin recovery, as well as a painless and bloodless sensation for the user. To form a rear side master, a PVC petri dish was also milled with a custom geometry.

A replica moulding process (Fig. 2) [34] was used to copy these master templates and to manufacture PDMS (Sylgard 184, Dow Corning, MI, USA) moulds: the two components of the PDMS kit were mixed in a 10:1 ratio, poured on the masters, degassed and finally peeled away. The front mould formed the negative copy of the MNs (Fig. 2A). The rear mould divided the resulting wafer into individual arrays (Fig. 2B), detachable by finger pressure. For this work, the arrays were designed as circles with a diameter of 9 mm.

Similarly, the two components of a medical grade epoxy (Epotek 353ND from Epoxy Technology, MA, USA) were mixed in a 10:1 ratio, poured on the front mould, spread to cover the entire surface, and degassed inside a vacuum chamber. The rear mould was then placed on the front mould and used to sandwich the epoxy in between. To ensure proper filling of the MNs holes, the stack was placed on a vacuum table for one hour and then oven cured at 80° C. Finally, the wafer was left to cool down to reach room temperature and the moulds peeled away (Fig. 2C).

The polymeric wafer was then metallized front and back with 20 nm

Table 1
MN type, production method, metallization, passivation, and application for several MN-based diagnostic devices.

MNs	Production	Metallization	Passivation	Application
280 μm PMMA (NOA 68)	Replica moulding	Thermally evaporated Au	Spin-coated PMMA (NOA 68)	Glucose sensing [19,28]
600 μm stainless steel	Wet etching	Electroplated Au and electrodeposited Pt-black	5 μm parylene coating	Glucose sensing [29]
500 μm stainless steel (SUS304)	Not specified	Electroplated Au	Electrochemical formation of AuZn oxide	Glucose sensing [22]
1 mm poly(carbonate)	Injection moulding	E-beamed Au and Ag	Syringe-deposited insulating varnish	B-Lactam antibiotic continuous concentration monitoring [23,24]
550 μm stainless steel (316 L)	Etching steel and punching out the MNs	Electroplated Au	Chemical vapour deposition of 5 μm of parylene	ECG monitoring [26]
70 μm polyimide	Casting in silicon etched master	Sputtered Pt	4–10 μm spin coated polyimide (PI-2732)	Neural interfacing [20]
60 μm glass	Wet etching	Deposited Pt	5 μm deposited SU-8	Neural interfacing [20]
320 μm silicon	Wet etching	Sputtered Au	8 μm parylene coating	EEG monitoring [30]
80 μm silicon	Deep reactive ion etching	Sputtered Au/Pt	5 μm parylene coating	Invasive neural electrical stimulation and recording [27]
500 μm Epotek 353ND	Replica moulding	E-beamed Ti/Pt and Ti/Ni/Ag	55 μm thick medical tape	Lactate amperometric detection [14]
700 μm carbon-loaded polystyrene	Micro-moulding	Electrochemically deposited Ag (only on reference MNs)	Enamel coating	pH measurement [25]
250 μm OrmoComp	Moulding	AC/DC sputtered Au	Spin coated OrmoComp (2 μl)	pH monitoring [21]

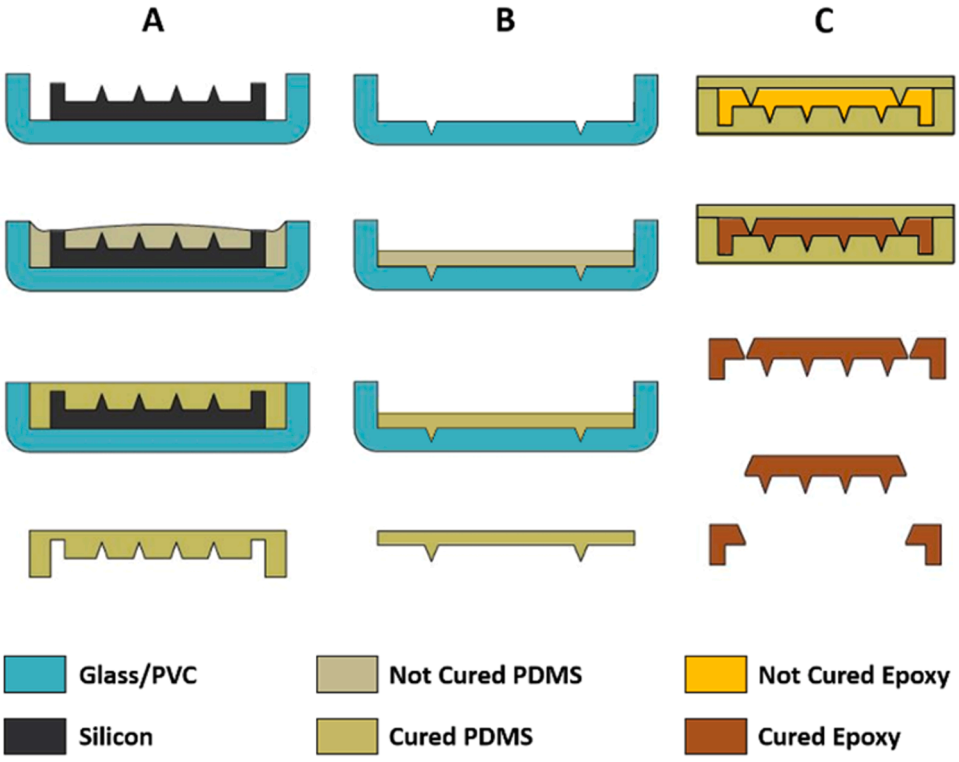


Fig. 2. MNs production process schematic: front (A) and back (B) moulds are fabricated from the master templates. The moulds are then used to produce a polymer MNs wafer (C). Reproduced under the terms of the CC-BY 4.0 license from ref [32], Copyright 2022, the Authors, published by IEEE.

of titanium (Ti), functioning as an adhesion layer, and 100 nm of platinum (Pt). A Temescal EUFC4900 (Ferrotec, USA) e-beam deposition tool was used for the metallization. The geometry of the back mould enabled through-wafer electrical connection and divided the wafer into 17 circular electrodes, each with a diameter of 9 mm. Fig. 3 shows one of these metallized circular arrays.

2.2. Microneedle array passivation

In this study, layer thicknesses as well as deposition and patterning methods were based on literature reviews and commonly available microfabrication techniques.

The arrays were passivated using six different materials: Maybelline 130 varnish (Maybelline, New York, USA), 600 nm silicon oxide, A15 PMMA (from EM Resist, Manchester, England), Epotek 353ND (from Epoxy Technology Europe GmbH, Augsburg, Germany), a 55 μm thick medical-grade tape (ARcare 7759 from Adhesives Research, Limerick, Ireland) and a 2 μm thick parylene layer.

The varnish was directly brushed over the MN array. The tips of the needles were exposed due to gravity as the wet varnish flowed back towards the substrate. Once the first layer of varnish was dry, a second layer was applied in the same manner. This method is expected to create a coating with a thickness greater on the substrate than on the lower body of the needle.

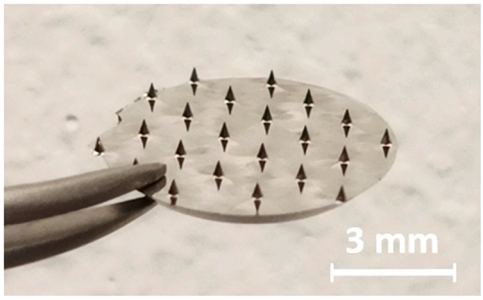


Fig. 3. 9 mm metallized circular MN array.

SiO_2 was deposited and patterned at wafer level using an existing double masked sputtering process. An aluminum shadow mask was machined using a VMC (Vertical Machining Centers) tool. This mask was a 100 mm disk composed of 1 mm wide metal bars separated by 0.75 mm wide openings. The mask was positioned on the wafer so that the bars were aligned with and covering all MN rows (Fig. 4A and 4B). A 300 nm oxide layer was then deposited on the wafer (Fig. 4C). The mask was then separated from the wafer, rotated 90° (Fig. 4D) and the sputtering repeated once more (Fig. 4E). Theoretically, the double deposition passivated the entire surface except for 1×1 mm^2 squares centered on each needle (Fig. 4F). Sputtering should allow the deposition of very thin and conformal layers, potentially maximizing the amount of usable height.

SiO_2 is also commonly implemented in various microelectronics applications, and it is known to be a very stable passivation layer. It resists several chemical and thermal processes, it is a good electrical insulator, and it is a great barrier against impurities [35]. It is resistant to corrosion and abrasion, it is resistant to microorganisms colonization, and thin layers of SiO_2 are very flexible [36]. All these characteristics make sputtering of SiO_2 very appealing as a potential candidate material for MN passivation.

Both PMMA and Epotek were spin-coated on the arrays using an OPTIcoat ST30 coater from ATMvision (Singen, Germany). In both cases, the arrays were washed with acetone and blown dry with nitrogen prior to coating. The spin-coating profile for PMMA was 100 rpm for 2 s, followed by 500 rpm for 2 s and 1400 rpm for 45 s. The material was then baked at 150° C for 3 min on a hotplate. The Epotek was pre-heated at 50° C to decrease the viscosity and spun at 500 rpm for 2 s followed by 1000 rpm for 2 s and 2500 rpm for 45 s. Finally, the epoxy was baked for 2 min at 150° C. Spin coating should help to improve the uniformity of the coating over more manual techniques such as brushing (as used for varnish). However, the MNs are 3D structures. Therefore, they could interact with the coating process in a manner that may lead to different thicknesses on opposite sides of each needle. The spin coating recipes have been selected following testing of different spinning parameters. These tests have been included as supplementary information. Both PMMA and epoxies have good stability [37,38], and ISO certified medical-grade options, making them promising candidates for passivating biosensors.

ARcare 7759 is a single-sided acrylic pressure-sensitive adhesive (PSA) on a clear polyester backing. After removal of the release liner, the backing/adhesive layers have a combined nominal thickness of 55 μm (25 μm for the backing and 30 μm for the AS-110 medical grade acrylic adhesive). The tape was cut to shape and patterned with 500 μm circular holes using a Graphtec CE7000–40 vinyl cutter. The holes were centered over each MN. The adhesive layer was manually applied to each array and pressed down with tweezers to properly attach it to the substrate. ARcare is the thickest passivation layer and will not cover the lower region of the MNs. However, it should be durable and mechanically very stable. The adhesive layer is a certified medical grade material, and this tape has already been used for *in-vivo* studies [31], proving its biocompatibility. As demonstrated by the production of perforated tapes for products such as wound dressings, patterning of tape is also scalable at industrial level. These qualities make this passivation technique very appealing for use on MN-based biosensors.

Prior to parylene coating, the back of the wafer was protected by applying Kapton polyimide tape (Farnell, Ireland) (Fig. 5A and 5B). The front of the wafer was passivated with a 2 μm thick layer of parylene (Fig. 5C) using a Labcoater 3 Parylene Deposition System (PDS 2010 from Specialty Coating Systems, Indianapolis, USA). The protective tape was then removed from the back of the wafer (Fig. 5D), and the individual arrays detached from the wafer frame. Using the vinyl cutter, a Kapton sheet (Farnell, Ireland) was perforated with 500 μm circular openings positioned to correspond with the MNs. Individual pieces were cut to match the shape of the arrays. The Kapton sheet was then placed on the arrays (Fig. 5E and 5F). The metal masks described earlier were used to function both as heatsinks and as a clamping mechanism, firmly locking this sheet against the array (Fig. 5G). The parylene was finally etched from the exposed needles and surrounding circular areas with 4 cycles of plasma oxygen (Fig. 5H), exposing the Pt (Fig. 5I). The plasma

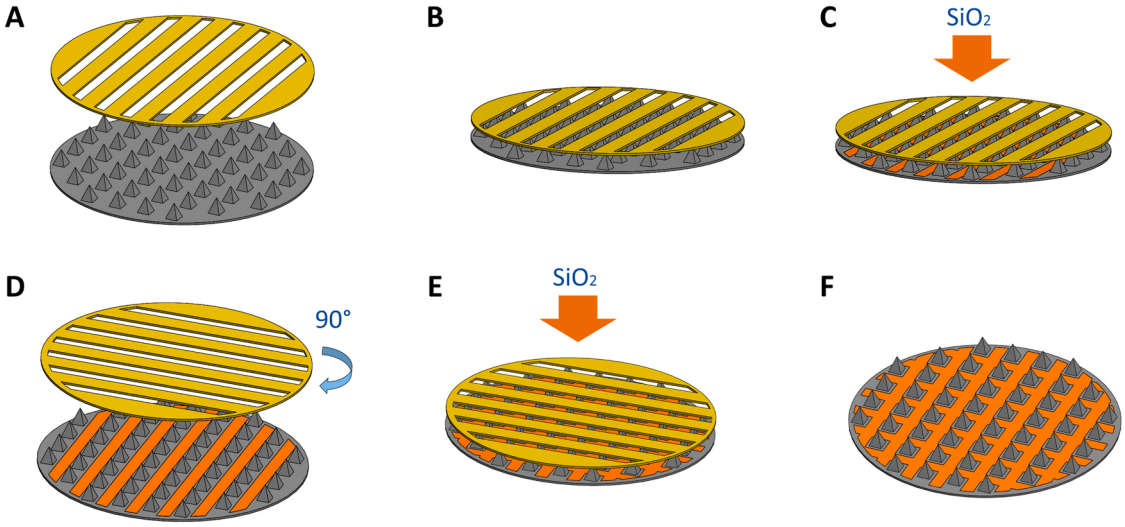


Fig. 4. Schematic of the SiO_2 deposition process: the MN wafer was coupled with the metal mask (A) so that the needles were protected (B). SiO_2 was then sputtered on the wafer (C). The mask was rotated 90 degrees (D) and the process repeated (E), passivating the wafer except for 1×1 mm^2 squares around centred on the MNs (F).

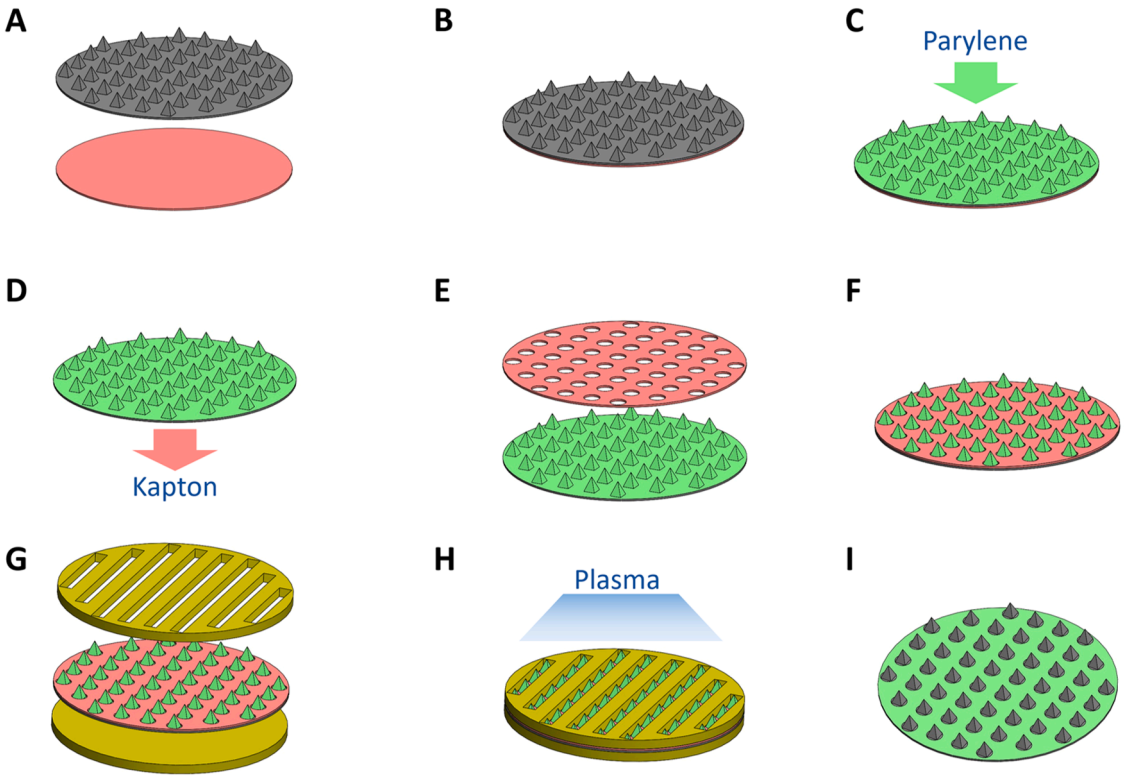


Fig. 5. Schematic of the parylene passivation: Kapton tape was used to protect the back of the wafer (A and B) and parylene was then deposited on the front (C). The tape was removed (D) and a Kapton sheet was cut, placed on the MN arrays (E and F) and sandwiched in between metal masks (G). The parylene was then plasma etched (H) to expose the needles and circular areas around them (I).

was generated using 285 W power, 23 mL/min of oxygen and delivered by a March Plasmod plasma asher (March Instruments Incorporated, acquired by Nordson, Ohio, USA). The first 3 cycles were 5 min long while the last plasma cycle was 3 min long. At the end of each one of them, the samples were blown with nitrogen and left to cool down at room temperature to minimize thermal stresses. In a manner similar to SiO_2, parylene should form a thin, precise, and conformal layer. Hence, the available height usable for penetration should be maximized. Also, it is widely used for medical devices due to its excellent biocompatibility, corrosion resistance, and long-term stability [39,40]. Therefore, parylene would be more appealing than SiO_2. However, the additional etching step makes the process more complex. Still, both plasma etching [41] and chemical vapor deposition [42] are used at industrial level, making this technique fully scalable.

2.3. Microneedle testing

All arrays were visually inspected using both an optical microscope and a Zeiss Supra 40 scanning electron microscope (SEM). Using data combined from both techniques, the average exposed area was calculated for each passivation method.

To electrochemically evaluate and compare all samples, the arrays were mounted on 3D printed supports equipped with electrical connection (Fig. 6).



Fig. 6. MN array mounted on a 3D printed support with electrical connectivity.

The supports were printed with a Formlab 3+ printer (Solid Print3D Ltd, UK) and white resin (F2GPWH04 from Solid Print3D Ltd, UK). The arrays were attached to the supports using 8330S conductive glue (MG Chemicals, Manchester, UK). All gaps in between the two parts were completely sealed using Loctite Power Flex superglue (Henkel Corp., OH, USA).

Cyclic voltammetry (CV) was employed to characterize the samples: the arrays were used as a working electrode (WE) together with an external Ag/AgCl reference electrode (RE - Gamry, Warminster, PA 18974, USA) and a Pt wire (Gamry Instruments, PA, USA), functioning as counter electrode (CE). The measurements were performed at room temperature with an Autolab MAC90389 electrochemical workstation (Metrohm, Cheshire, UK) using a NOVA 2.1 software and a Faraday cage (Metrohm).

The CV scans were performed in a 10 mM PBS solution (pH = 7.4) containing 1 mM FcCOOH, sweeping between 0 and 0.6 V with a 0.05 V/s scan rate. The arrays were cleaned prior to characterization with CV scans executed in a H_2O: NH_4Cl: H_2O_2 solution (5:1:1 ratio). The potential of the cleaning CV was cycled between −0.5 V to 0.5 V using a scan rate of 0.05 V/s versus the Ag/AgCl *Re* and the Pt CE.

Ammonium chloride (NH_4Cl), ferrocenemonocarboxylic acid (FcCOOH) and phosphate buffered saline (PBS) were all acquired from Merck (Sigma Aldrich, Arklow, Ireland). Milli-Q water (H_2O; resistivity 18.2 MΩ.cm) was use as solvent for all solutions.

The surface properties of passivation layers, particularly hydrophobicity, play a critical role in influencing biomolecule adhesion and subsequent electrochemical performance. To evaluate this, contact angle measurements were performed for each passivation layer. They were carried out using an OCA20 wetting angle kit by DataPhysics Instruments GmbH (Filderstadt, Germany). Three samples were used for each layer.

3. Results

A primary objective of adding a passivation layer is to isolate the substrate area while allowing as much of the needle body as possible to remain in contact with the epidermal layers. Therefore, both SEM and optical microscopy images were analysed to calculate the total exposed area of the arrays after application of the various layers. ImageJ [43] was used to perform the analysis of the pictures. The optical microscope images were used to check for defects in the passivation layers covering the substrate and, if present, to determine the exposed area around the needles. On the other hand, SEM was essential to accurately evaluate the non-passivated percentage of the lateral surface of the MNs. Six MNs for each passivation technique were used to calculate an average unprotected area. This value was used to estimate the total exposed area for each array passivated with the same method. Fig. 7 shows an example of the passivated MNs compared with a bare needle. The MNs shown in the pictures are 500 μm tall. An image of the SiO_2 sample was not included in Fig. 7 because no evident visual differences with the control were observed.

The MNs are shaped as octagonal pyramids. Therefore, the lateral surface area, A_l and the base area A_b, can be calculated using the following formulas:

$$A_l = 2s\sqrt{4h^2 + s^2 cot^2\left(\frac{\pi}{8}\right)} \tag{1}$$

$$A_b = 2s^2 cot\left(\frac{\pi}{8}\right) \tag{2}$$

where s is the base edge length and h is the pyramid height.

Considering Fig. 7, the MNs covered with varnish exhibited a shape more similar to a cone. Therefore, for this specific passivation, A_l was calculated using:

$$A_l = \pi r l \tag{3}$$

where r is the base radius of the cone and l is its slant height.

The average values found for h and s together with the corresponding calculated lateral areas are reported below in Table 2. The values reported for varnish are l instead of h and r instead of s (highlighted in the table itself close to the number).

Six arrays were analyzed and tested for each passivation method. Due to the circular nature of the MN samples and the positioning of the rear mould, the number of needles on each array may vary from sensor to sensor. The average number of MNs on each array was 18 ± 3. The theoretically exposed surface area (*TSA*) was calculated for each electrode. Varnish, PMMA and Epotek only used the lateral unprotected area (A_l) and multiplied it by the number of needles on the array. ARcare

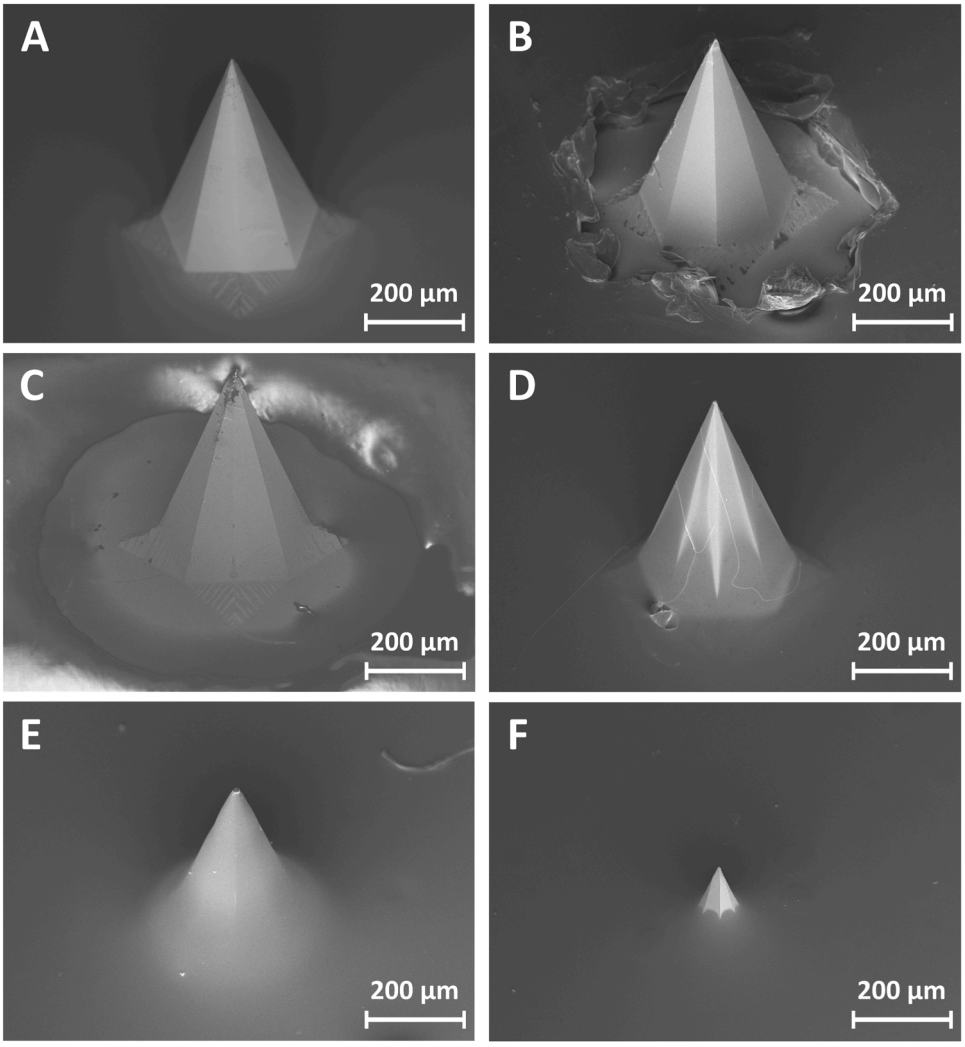


Fig. 7. SEM images of a bare MN (A) together with all passivated needles. The passivation captured are ARcare 7759 (B), parylene (C), PMMA (D), varnish (E) and Epotek (F) respectively. No evident difference was observed between SEM pictures of control and SiO_2 passivated MNs.

Table 2
Average values for h, s, A_l and A_{ex} are calculated for each passivation technique ($n = 6$ for each cases). For the varnish, l and r are reported instead. The theoretical surface area (TSA) of the exposed portion of the differently passivated arrays is reported in the last column.

Passivation	*h* (μm)	*s* (μm)	A_l (mm^2)	A_{ex} (mm^2)	*TSA* (mm^2)
Control	500 ± 5	124 ± 2	0.259 ± 0.007	All exposed	55.2 ± 0.8
SiO_2	500 ± 5	124 ± 2	0.259 ± 0.007	0.625 ± 0.375	18 ± 12
Parylene	500 ± 5	124 ± 2	0.259 ± 0.007	0.45 ± 0.02	9.5 ± 0.5
ARcare 7759	500 ± 5	124 ± 2	0.259 ± 0.007	0.17 ± 0.01	6.4 ± 0.4
PMMA	359 ± 16	92 ± 4	0.14 ± 0.01	0	2.4 ± 0.3
Varnish	191 ± 33, *l*	60 ± 10, *r*	0.05 ± 0.02	0	0.8 ± 0.3
Epotek 353ND	131 ± 14	32 ± 12	0.017 ± 0.009	0	0.3 ± 0.2

7759 and parylene followed the same procedure. However, before multiplying by the number of MNs, the exposed substrate area (A_{ex}) minus the base area of the octagonal pyramids (A_b) was added to A_l. A_{ex} was calculated once again by analyzing six SEM pictures with ImageJ and averaging the results. The circular exposed substrate areas were 0.46 ± 0.02 mm^2 and 0.17 ± 0.01 mm^2 for the parylene and ARcare 7759 respectively. The same steps were followed for the SiO_2. However, it was difficult to clearly see the pattern of the deposited oxide because of the thin and transparent nature of the material. Therefore, for this passivation, A_{ex} was calculated starting from the 1 mm^2 square theoretically produced by the double sputtering process. Because the sputtering was performed with the mask not in hard contact with the substrate, the oxide was likely to spread underneath the mask [44], covering more area than intended (Fig. 8).

From our previous experience with sputtering metals on masked MN wafers [31], the side of the exposed square could be reduced from a nominal value of 1 mm to as little as 0.5 mm. The spreading would form a layer decreasing in thickness with distance under the mask. This would also explain the difficulties encountered while trying to visually identify a clear distinction between the sputtered and the unprotected area. Considering the possible side reduction, A_{ex} could vary between 1 mm^2 and 0.25 mm^2. Therefore, A_{ex} was considered as 0.625 ± 0.375 mm^2.

After finding all A_l and A_{ex}, six different arrays were prepared for every passivation. The average exposed area was then calculated for each different type of array as explained. If any defect was spotted in the passivation, this additional area (*AA*) was averaged and added to the total unprotected area. Therefore, *TSA* was calculated as follows:

$$TSA = (A_l + A_{ex} - A_b)MNs + AA \quad (4)$$

where *MNs* is the number of needles on the array.

As stated, for PMMA, varnish and Epotek, A_{ex} and A_b were not used.

Possible sources of errors were taken into consideration for all dimensions. For the MNs where the passivation is not covering any part of the needles, the uncertainty in *h* and *s* is caused exclusively by the moulding process (control, SiO_2, parylene and ARcare 7759). If the MNs are partially covered, the standard deviation found while averaging the values taken from the SEM images was used instead (PMMA, varnish, Epotek). These errors were also propagated to calculate the possible variation for A_l. A_{ex} inaccuracy was either taken from the possible imprecision introduced by the passivation process (SiO_2) or from the standard deviation found from image analysis. The propagation of the error was also used to find the *TSA* uncertainty for each passivation. All data is summarized in Table 2.

In the context of passivated microneedles, electrochemical correlation can be important in understanding how the passivation layer affects the electrochemical properties of the microneedles.

Therefore, cyclic voltammetry was carried out on the six previously prepared sensors. This was done to evaluate the electrical isolation provided by the different passivation layers: the lower the observed currents are, the higher electrochemical isolation the passivation provides. Average electron transfer behavior results are reported in Fig. 9.

Understanding the electrochemical properties of passivated microneedles is important for optimizing their performance in various applications. Passivation layers significantly affect electron transport properties, especially in enzyme-modified sensors. As demonstrated by different studies [45,46], comparing different passivation methods provides valuable insights and offers a more thorough understanding of their impact. Oxidation and reduction peak currents, namely I_p^{ox} and I_p^{red}, total current variation (ΔI) and Electrochemical Surface Area (*ESA*) were extracted from the curves and are reported in Table 3.

The *ESA* was calculated starting from the following relation for I_p^{ox}

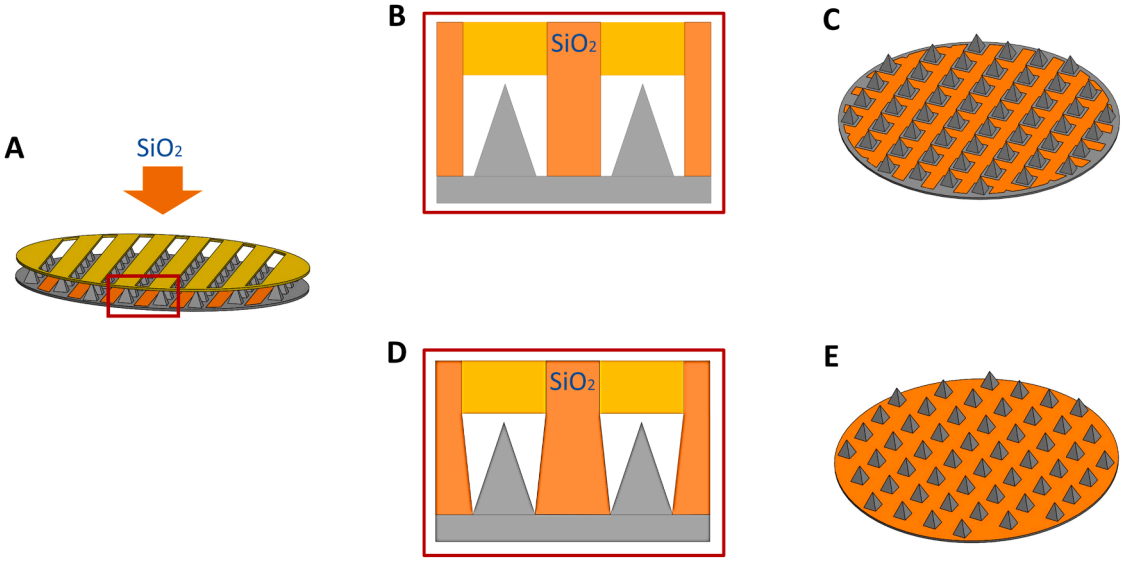


Fig. 8. Schematic representing the undesired spreading of the SiO_2 underneath the mask. This phenomenon has also been reported by other authors [44]. Once the sample was ready for sputtering, a gap was present between the tip of the MNs and the mask (A). Ideally, the oxide should have covered only the exposed area (B and C), however, it spread underneath the mask (D), covering more surface (E).

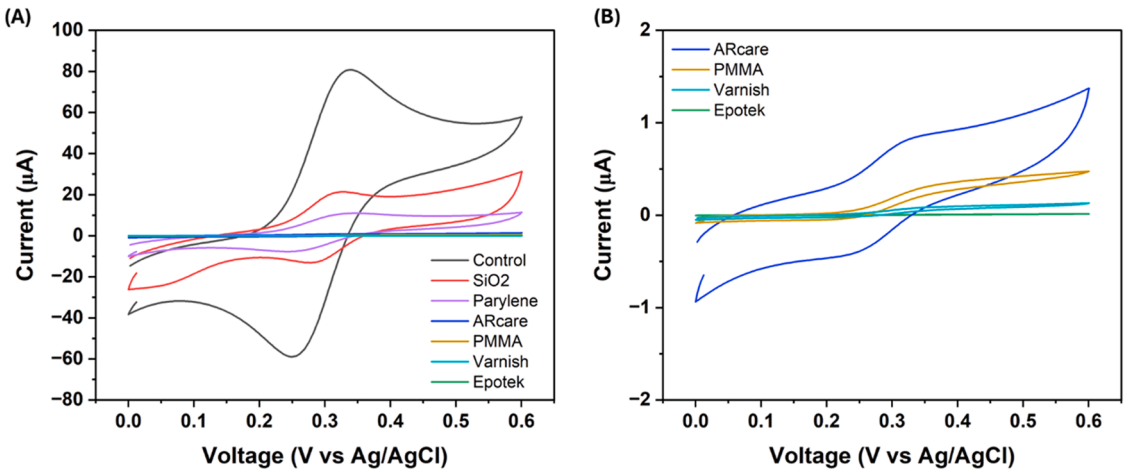


Fig. 9. CV scans in 1 mM FcCOOH in 10 mM PBS for each passivation method (A) together with magnification on the ARcare 7759, PMMA, varnish and Epotek curves (B).

Table 3
Peak currents (I_p^{ox} and I_p^{red}) and total current (ΔI) extracted from the graphs in Fig. 9. The ESA calculated from Eq. (6) is also reported.

	Peak Current (x 10^{-7} A)			
Passivation	I_p^{ox}	I_p^{red}	ΔI (μA)	*ESA* (mm^2)
Control	808 ± 113	−590 ± 84	140 ± 20	57.8 ± 0.8
SiO_2	214 ± 23	−131 ± 38	35 ± 6	15.3 ± 0.2
Parylene	172 ± 18	−133 ± 21	30 ± 4	12.3 ± 0.1
ARcare 7759	110 ± 10	−77 ± 11	19 ± 2	7.9 ± 0.1
PMMA	3.0 ± 0.5	−0.3 ± 0.2	0.33 ± 0.07	0.210 ± 0.004
Varnish	0.8 ± 0.1	−0.16 ± 0.05	0.10 ± 0.02	0.060 ± 0.001
Epotek	0.081 ± 0.02	−0.0003 ± 0.006	0.008 ± 0.003	0.0060 ± 0.0002

[47]:

$$I_p^{ox} = (2.69 \cdot 10^5) \cdot n^{\frac{3}{2}} \cdot ESA \cdot C \cdot D^{\frac{1}{2}} \cdot v^{\frac{1}{2}}, \quad (5)$$

where n is the number of electrons transferred in the redox, D is the diffusion coefficient of the oxidised analyte, C is the bulk concentration of the analyte and v is the used scan rate. For our system, $C = 10^{-3}$ mol/cm^3, $v = 0.05$ V/s, $n = 1$, $D = 5.4 \times 10^{-6}$ cm^2/s.

Therefore, the electrochemical surface area can be calculated as:

$$ESA = \frac{I_p^{ox} \cdot n^{-\frac{3}{2}} \cdot D^{-\frac{1}{2}} \cdot v^{-\frac{1}{2}}}{(2.69 \cdot 10^5) \cdot C}, \quad (6)$$

The imprecision for the *ESA* was calculated only considering the standard deviation of I_p^{ox}. In a perfect scenario, the *ESA* should correspond with the *TSA* recorded in Table 2. Therefore, the *ESA* was then compared with the previously calculated *TSA*. The values are reported in Table 4, along with the Ideal Surface Area (*ISA*). This is the product of the lateral surface area A_l multiplied by the number of needles per array. It represents the surface area that would result from application of an ideal passivation layer. This layer would cover the entire substrate area whilst allowing the total surface area of the needle to remain exposed.

Table 4
Comparison TSA calculated from the images analysis with the experimentally measured ESA. In addition, the average number of MNs is reported for each sample together with the total lateral MNs area on the samples (ISA).

Passivation	# MNs per array	*ISA* (mm^2)	*TSA* (mm^2)	*ESA* (mm^2)
Control	22	5.7 ± 0.2	55.2 ± 0.8	57.8 ± 0.8
SiO_2	17 ± 1	4.4 ± 0.1	18 ± 12	15.3 ± 0.2
Parylene	15 ± 1	3.9 ± 0.1	9.5 ± 0.5	12.3 ± 0.1
ARcare 7759	18 ± 1	4.7 ± 0.1	6.4 ± 0.4	7.9 ± 0.1
PMMA	17 ± 1	4.4 ± 0.1	2.4 ± 0.3	0.210 ± 0.004
Varnish	21 ± 1	5.4 ± 0.2	0.8 ± 0.3	0.060 ± 0.001
Epotek	19 ± 1	4.9 ± 0.1	0.3 ± 0.2	0.0060 ± 0.0002

These results were also plotted and are visually represented in Fig. 10.

It is immediately clear from Table 4 that the *TSA/ESA* varies strongly with passivation type. ARcare 7759 was the closest to its *ISA*. In addition, in some cases, significant differences were also observed between the *ESA* and *TSA* measurements. Therefore, each samples' group was individually inspected to find the cause of these variations.

Starting from the control, the *ESA* was slightly larger than what was initially estimated. From Fig. 11, it is evident that the superglue used to seal the mounted electrodes formed an irregular shape at the edges of the array. This made a precise assessment of the area more difficult while processing the images. Moreover, cyanoacrylate has the tendency to bloom [48], the effect of which will further increase any visual underestimation of the exposed area.

Overall, these phenomena easily explain the < 3 % difference found in between the *TSA* and *ESA* measured on control samples. Changing the adhesive or improving control over dispensing/environmental factors, could reduce this discrepancy even further [48].

SiO_2's *TSA* had a large uncertainty due to the potential spreading of the oxide below the mask. However, the measured *ESA* was also within this range and could be used to experimentally calculate the dimensions of the exposed area around the MNs. Firstly, for each needle, A_l was removed from the *ESA* and A_b re-added. Then *AA* was subtracted, and the remaining surface divided by the number of MNs. The number of needles for the SiO_2 samples was 17 ± 1. Considering this variability, the real A_{ex} for the SiO_2 process was calculated to be 0.47 ± 0.03 mm^2.

Both ARcare 7759 and parylene showed an *ESA* higher than the *TSA* and *ISA*, indicating a larger exposed area. Analyzing ARcare 7759 first, two possible causes were highlighted by the SEM analysis. Because of the relatively low resolution provided by the mechanical cutting process, the edges of the openings are not sharply defined (Fig. 12). Therefore, the standard deviation calculated for A_{ex} was probably an underestimation of the real variability of the hole size. Secondly, because the tape was placed on the arrays by hand, it was difficult to reliably ensure intimate contact between the passivation and the substrate (Fig. 12A). Partial lifting of the tape would expose more electroactive area, explaining the higher *ESA*.

Using a laser cutter instead of a vinyl cutter [14] would increase the reproducibility and precision of the layer. This would guarantee a more homogenous result, avoiding the irregular edges shown in Fig. 12.

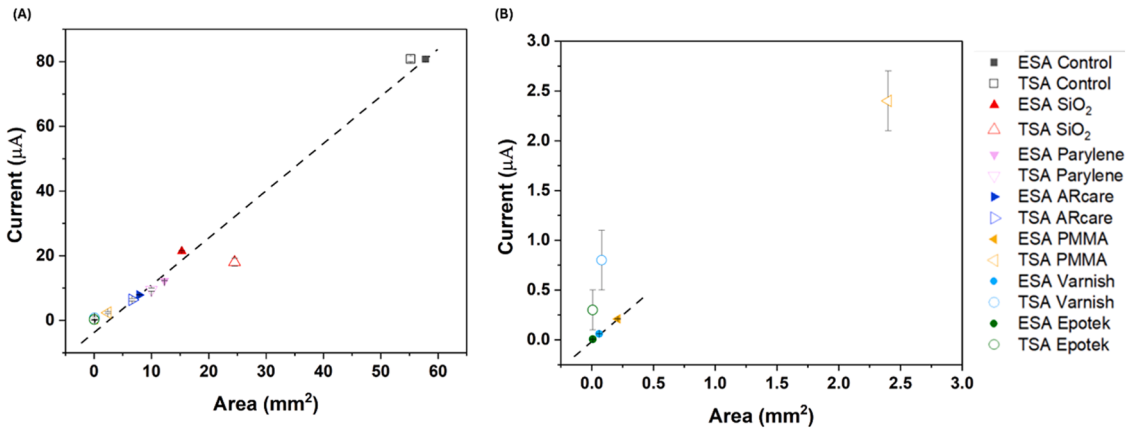


Fig. 10. Scatter plots of current vs area showing differences between the electrochemically found *ESA* (full marker) and visually measured *TSA* (empty marker). A dashed line was traced starting from the control to highlight the linear correlation between area and observed current (*ESA*). The second plot (B) focuses on the smaller values not clearly visible in the first one (A).

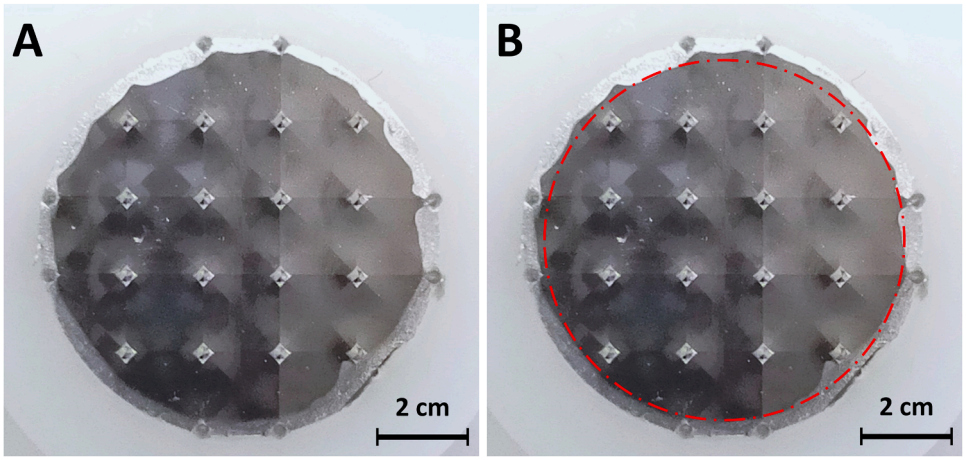


Fig. 11. Top view of a bare microneedle array assembled for electrochemical characterization (A). The red dashed circle has been included to highlight the irregularity of the superglue used to insulate the front of the electrode from the back (B).

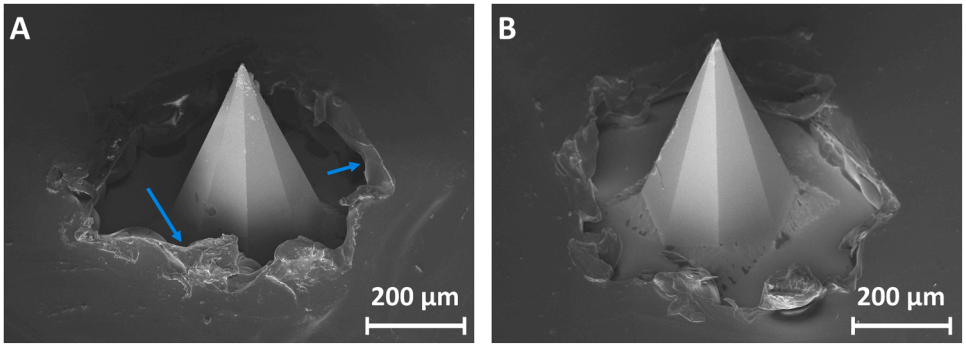


Fig. 12. SEM images of two ARcare 7759 passivated MNs. The first image (A) is showing the tape lifting (blue arrows) while, in the second case (B) the tape is in intimate contact with the substrate.

However, considering the possible risk of the lifting of the tape, this passivation may not be the best option for densely packed MN arrays.

The parylene passivated sensors were inspected next. Defects, highlighted by blue arrows on Fig. 13, were occasionally found alongside the rim of the passivation layer. These imperfections increased A_{ex}, explaining the original *TSA* underestimation. Considering they were all placed in similar positions over the parylene edges, this was more likely caused by the removal of the Kapton mask, which was peeled away from the array in the direction in which defects were subsequently found. Interestingly, the area calculated during the initial analysis reported in Table 2 was already showing parylene etching over a surface bigger than what the Kapton mask was leaving exposed. The parylene appeared to be removed over circles with a diameter of 754 μm (± 15 μm, $n = 6$) rather than the originally designed 500 μm, which we assume is due to under-etching below the Kapton mask.

The three liquid layers (PMMA, vanish and Epotek) showed exposed

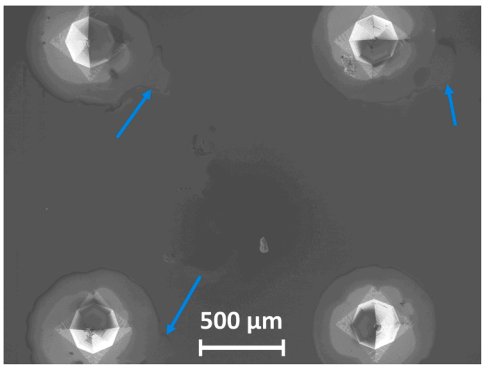


Fig. 13. Parylene passivated MNs after oxygen etching. Blue arrows are highlighting examples of defects that may occur at the edges of the parylene layer.

areas that were significantly smaller than those measured using the other methods. For varnish and Epotek, this area was near zero. The experimentally measured *ESA* of the Epotek passivated arrays was 55 times smaller than the expected *TSA*. Similarly, both PMMA and varnish also had very large differences between *ESA* and *TSA*. For Epotek passivation, it was immediately evident from the SEM and optical miscroscope images (Fig. 14) that the needle coverage was highly variable. Secondly, the polymer was not conformal to the MNs. It rather formed a thick layer over the entirety of the space in between needles, greatly reducing the height available for skin penetration. The *ESA* result showed that the exposed area was near zero. This indicates that the spin coating process may also result in a thin layer coating the entire needle, that was difficult to visually detect during *TSA* calculation.

The result could indicate the need to refine the spin coating profile. It could also mean that a thermal curing polymer, whose viscosity highly varies with temperature changes, may not be ideal for spin coating.

As shown in Fig. 15, the spincoated PMMA polymer layer was thinner and more conformal to the needles, allowing more of the structure to protrude above the passivation. However, considering the high discrepancy in between *TSA* and *ESA*, it is likely that a thin and visually undetectable layer of PMMA is covering a significant portion of the MNs.

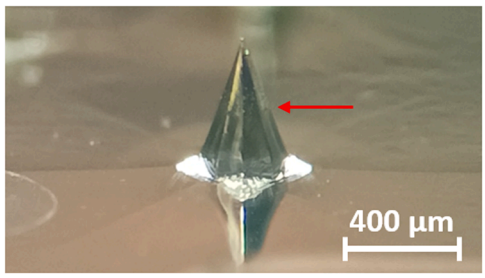


Fig. 15. Optic microscope image of a PMMA passivated MN. The red arrow is showing the possible edge of the passivation on the side of the needle. However, the difference is not clearly detectable.

The last remaining electrodes which needed deeper investigation were the varnish-passivated arrays. The SEM pictures showed a shape more similar to a cone than to a pyramid, already suggesting the presence of varnish high on the needles. High resolution optical microscopy was used to better assess the coverage of the needles. Varnish is clearly visible on the sides of the needles almost for the entirety of its height (Fig. 16). Contrarily to what was assumed using the SEM, the only evidently exposed areas seemed to be the tip and the intersections between the lateral faces of the octagonal pyramid. This reduced area is likely to be the reason of the overestimation in *TSA* compared to *ESA*. Like PMMA, varnish was conformal to the shape of the needles.

The results of the contact angle measurements are reported in Table 5.

Hydrophobicity reduces biomolecule adhesion. This was shown by Yan et al. which demonstrated that hydrophobic self-assembled monolayers (SAMs) can enhance direct electron transfer by minimizing undesired surface interactions [49]. Conversely, more hydrophilic surfaces demonstrate increased biomolecule adhesion [50]. As shown by Heydari-Bafrooei and Ensafi, this can enhance electron transfer efficiency by promoting effective biomolecule immobilization [51]. However, this increased adhesion may also lead to non-specific adsorption of unwanted species, causing higher background noise and reduced signal reproducibility [52].

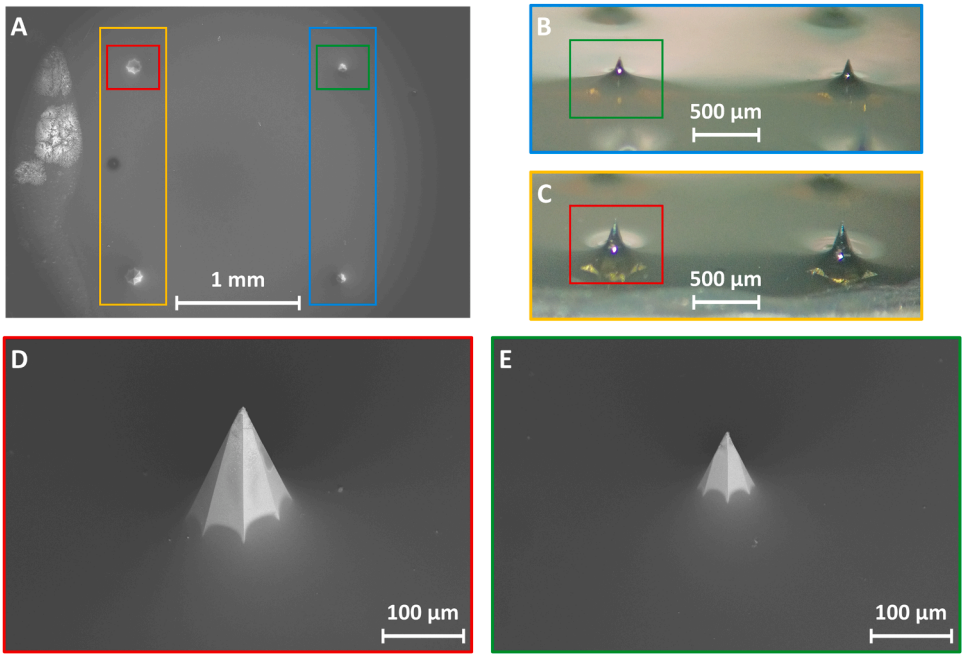


Fig. 14. SEM images of an Epotek passivated array (A) together with close up views of 2 MNs (D and E). Optical microscope images of the same needles are reported as well (B and C). Colour coding was used to better show correlations between different images.

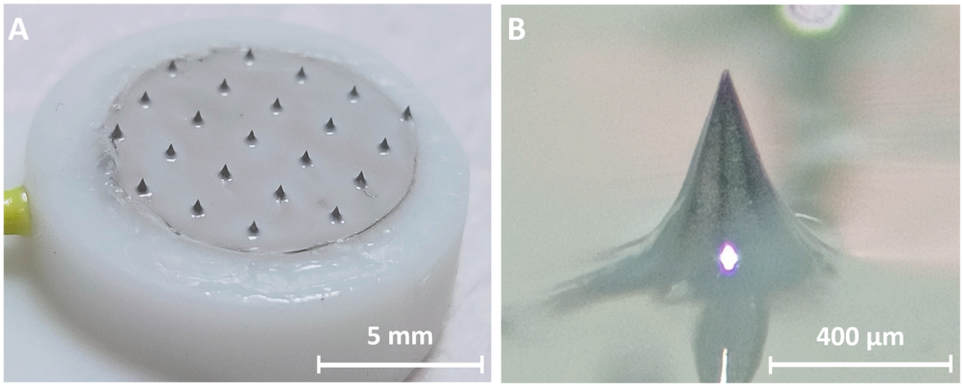


Fig. 16. Picture of a varnish passivated array (A) and 75° angled optical microscope magnification of an individual needle (B).

Table 5
Contact angled measured for the different passivation layers.

Passivation	Contact angle (°)
Control	45.0 ± 2.8
ARcare 7759	29.8 ± 1.8
Parylene	39.4 ± 1.1
PMMA	45.1 ± 2.4
Epotek	52.2 ± 2.8
Varnish	64.3 ± 1.1
SiO_2	65.35 ± 1.2

4. Discussion and conclusions

Passivation layers are an essential component of microneedle-based biosensor devices, and are used to block responses arising from the unwanted functionalisation of the substrate around the needles. In this paper, we have firstly provided a definition of an ideal passivation layer, and then carried out a preliminary study of six potential passivation materials.

Three liquid layers - PMMA, varnish and Epotek 353ND - were found to result in coatings difficult to control. These led to low or near-zero exposed areas in all three cases. Uniformity of the coverage, together with high difference between *ESA* and expected *TSA*, was also a concern. Significant additional work is required to optimise the coating procedures and to render these materials a viable option for passivation. Direct brushing is relatively uncontrollable and, critically, not scalable. This makes it an inferior option to spin coating. Finally, spinning of Epotek resulted in a dramatic reduction of the height available for skin penetration, making this particular passivation process unusable. Therefore, the choice of the spin coating material is also critical to achieve more controllable results.

While sputtered silicon oxide may be used to passivate the substrate area, this method is prone to spreading of the material beneath the mask, covering more area than intended. This led to a significant difference between *ESA* and *ISA*. Further refinement, by either finding a way to control this spreading effect or by avoiding it altogether, would greatly improve the resolution of the deposited pattern. SiO_2 is highly stable, and sputtering is an industrially viable deposition option. Therefore, a solution to this problem could potentially make the sputtering of this oxide one of the best techniques for biosensor passivation. We have recently reported early progress in this regard, developing wall-like features which could potentially help in solving this issue [31]. Also, although some studies have shown promising results for SiO_2 use *in-vivo* applications, detailed biocompatibility studies should also be conducted to further reinforce their usability [36].

Parylene and Arcare 7759 seemed to be the best performing passivation materials, with experimentally measured and theoretical exposed areas of similar size. Parylene deposition resulted in a thin, reliable and controllable covering. However, its use would still benefit from a deeper understanding of the etching process, together with a refinement of the masking mechanism. This could also enable a more accurate covering of the substrate, resulting in an *ESA* closer to the *ISA*. Whilst medical tape is relatively thick, reducing the height of the needle available for penetration, it can be mechanically applied without the need for specialised deposition or etching tools. Laser cutting could be used to greatly improve the fidelity of the pattern on the tape in a scalable manner. The hole size could also be increased to facilitate a better contact between substrate and passivation, but this would come at a higher difference in between *ESA* and *ISA*. Finally, the single faced tape used in this work could be replaced with a double-sided tape, thereby providing a method of ensuring skin adhesion as well as sensor passivation. To be fully industrially viable, a custom machine should be used to reliably apply the tape to the arrays in a repeatable and automatic fashion.

Surfaces of increased hydrophobicity reduce biomolecule adhesion, which may result in improved signal stability and reduced surface fouling during electrochemical measurements. However, hydrophilic surfaces enhance biomolecule adhesion, improving electron transfer efficiency. Therefore, optimizing the hydrophobicity of passivation layers is essential to balance effective biomolecule adhesion with favourable electron transport properties. For enzyme-modified sensors, moderate hydrophobicity may provide an optimal compromise between enhancing electron transfer efficiency whilst minimizing interference from non-specific adsorption. Integrating this approach with advanced surface modification techniques may offer promising solutions for improving sensor performance in various biosensing applications.

While a number of teams have reported various materials and techniques, no commonly accepted standard for MN biosensor passivation exists, and so this work performed a preliminary study of use-case driven passivating materials and methods. In this manner, we hope to provide a basis for accelerating research in this important topic. Although a number of promising options have been developed, the high variability observed across the various methods and materials investigated here highlights the need for further research and process development in this area.

CRediT authorship contribution statement

Andrea Bocchino: Writing – review & editing, Writing – original draft, Visualization, Validation, Methodology, Investigation, Formal analysis, Data curation, Conceptualization. **Sofia Rodrigues Teixeira:** Writing – review & editing, Writing – original draft, Visualization, Validation, Supervision, Methodology, Investigation, Formal analysis, Data curation. **Fiona Barry:** Writing – review & editing, Validation, Investigation, Data curation. **Chinmay Thatte:** Writing – review & editing, Validation, Investigation, Data curation. **Adam Ryan:** Writing –

review & editing, Validation, Investigation, Data curation. **Fahima Rahman:** Writing – review & editing, Validation, Investigation, Data curation. **Yuan Hu:** Writing – review & editing, Visualization. **Simone Iadanza:** Writing – review & editing, Validation, Resources, Investigation. **Paul Galvin:** Writing – review & editing, Supervision, Resources, Project administration. **Steffen Kurzhals:** Writing – review & editing, Methodology, Conceptualization. **Eva Melnik:** Writing – review & editing, Methodology, Conceptualization. **Giorgio C. Mutinati:** Writing – review & editing, Resources, Project administration, Funding acquisition, Conceptualization. **Conor O'Mahony:** Writing – review & editing, Supervision, Resources, Project administration, Methodology, Funding acquisition, Conceptualization.

Declaration of competing interest

The authors declare that they have no known competing financial interests or personal relationships that could have appeared to influence the work reported in this paper.

Acknowledgment

This work was funded by the European Union's Horizon 2020 research and innovation programme under Grant #825549 (ELSAH project); by Enterprise Ireland and the Chips Joint Undertaking ('Newlife', Grant Agreements IRF/2022/0066 and #101095792); by Research Ireland through the Insight Centre for Data Analytics (SFI/12/RC/2289-P2); by the Higher Education Authority through the Programme for Research in Third-Level Institutions; and by the European Regional Development Fund. For the purpose of Open Access, the author has applied a CC BY public copyright licence to any Author Accepted Manuscript version arising from this submission. Open access funding is provided by IReL.

Supplementary materials

Supplementary material associated with this article can be found, in the online version, at doi:10.1016/j.snr.2025.100328.

Data availability

Data will be made available on request.

References

[1] C. Kolluru, M. Williams, J. Chae, M.R. Prausnitz, Recruitment and collection of dermal interstitial fluid using a microneedle patch, Adv. Healthc. Mater. 8 (2019) 1801262, https://doi.org/10.1002/adhm.201801262.
[2] R.H. Stewart, A modern view of the interstitial space in health and disease, Front. Vet. Sci. 7 (2020), https://doi.org/10.3389/fvets.2020.609583. Article 609583.
[3] Y. Marunaka, The proposal of molecular mechanisms of weak organic acids intake-induced improvement of insulin resistance in diabetes mellitus via elevation of interstitial fluid pH, in: Int. J. Mol. Sci, 19, 2018, https://doi.org/10.3390/ijms19103244. Article 10.
[4] W. Pan, S. Xu, X. Mao, T. Li, Q. Cao, X. Ye, B. Liang, An integrated stretchable sensing patch for simultaneously monitoring of physiological and biochemical parameters, in: Proc. - IEEE Int. Conf. Nano/Micro Eng. Mol. Syst, IEEE, 2021, pp. 762–767, https://doi.org/10.1109/NEMS51815.2021.9451353.
[5] S.A. Byrnes, B.H. Weigl, Selecting analytical biomarkers for developing diagnostic technologies for global health applications: conference topics — Healthcare (medical technology), in: Proc. - IEEE Glob. Hum. Tech. Conf, IEEE, 2017, https://doi.org/10.1109/GHTC.2017.8239264, 1–1.
[6] P.P. Samant, M.M. Niedzwiecki, N. Raviele, V. Tran, J. Mena-Lapaix, D.I. Walker, E.I. Felner, D.P. Jones, G.W. Miller, M.R. Prausnitz, Sampling interstitial fluid from human skin using a microneedle patch, Sci. Transl. Med. 12 (2020) eaaw0285, https://doi.org/10.1126/scitranslmed.aaw0285.
[7] K.M. Saifullah, Z. Faraji Rad, Sampling dermal interstitial fluid using microneedles: a review of recent developments in Sampling methods and microneedle-based biosensors, Adv. Mater. Interfaces 10 (2023) 2201763, https://doi.org/10.1002/admi.202201763.
[8] F.K. Aldawood, A. Andar, S. Desai, A comprehensive review of microneedles: types, materials, processes, characterizations and applications, Polymers (Basel) 13 (2021) 2815, https://doi.org/10.3390/polym13162815.
[9] X. Zhang, Y. Wang, J. Chi, Y. Zhao, Smart microneedles for therapy and diagnosis, Research 2020 (2020) 1–26, https://doi.org/10.34133/2020/7462915.
[10] S. Dharadhar, A. Majumdar, S. Dhoble, V. Patravale, Microneedles for transdermal drug delivery: a systematic review, Drug Dev. Ind. Pharm. 45 (2019) 188–201, https://doi.org/10.1080/03639045.2018.153949.
[11] J. Yang, J. Yang, X. Gong, Y. Zheng, S. Yi, Y. Cheng, Y. Li, B. Liu, X. Xie, C. Yi, L. Jiang, Recent progress in microneedles-mediated diagnosis, therapy, and theranostic systems, Adv. Healthc. Mater 11 (2022) 2102547, https://doi.org/10.1002/adhm.202102547.
[12] R. Amarnani, P. Shende, Microneedles in diagnostic, treatment and theranostics: an advancement in minimally-invasive delivery system, Biomed. Microdevices 24 (2022) 4, https://doi.org/10.1007/s10544-021-00604-w.
[13] J. Madden, C. O'Mahony, M. Thompson, A. O'Riordan, P. Galvin, Biosensing in dermal interstitial fluid using microneedle based electrochemical devices, Sens. Bio-Sens. Res. 29 (2020) 100348, https://doi.org/10.1016/j.sbsr.2020.100348.
[14] S. Kurzhals, E. Melnik, P. Plata, E. Cihan, P. Herzog, A. Felice, A. Bocchino, C. O'Mahony, G.C. Mutinati, R. Hainberger, Detection of lactate via amperometric sensors modified with direct electron transfer enzyme containing PEDOT:PSS and hydrogel inks, IEEE Sens. Lett. 7 (2023) 1–4, https://doi.org/10.1109/LSENS.2023.3307066.
[15] M.-N. Chien, Y.-J. Chen, C.-H. Bai, J.-T. Huang, Continuous glucose monitoring system based on percutaneous microneedle array, Micromachines (Basel) 13 (2022) 478, https://doi.org/10.3390/mi13030478.
[16] J.J. García-Guzmán, C. Pérez-Ràfols, M. Cuartero, G.A. Crespo, Toward In vivo transdermal pH sensing with a validated microneedle membrane electrode, ACS Sens 6 (2021) 1129–1137, https://doi.org/10.1021/acssensors.0c02397.
[17] D. Terutsuki, S. Yamaguchi, Y. Abe, H. Abe, M. Nishizawa, Porous microneedle-based potentiometric sensor for intradermal electrolyte monitoring, Electrochemistry 91 (2023), https://doi.org/10.5796/electrochemistry.23-00027, 047007–047007.
[18] A. Ripolin, J. Quinn, E. Larrañeta, E.M. Vicente-Perez, J. Barry, R.F. Donnelly, Successful application of large microneedle patches by human volunteers, Int. J. Pharm. 521 (2017) 92–101, https://doi.org/10.1016/j.ijpharm.2017.02.011.
[19] C. Barrett, K. Dawson, C. O'Mahony, A. O'Riordan, Development of low cost rapid fabrication of sharp polymer microneedles for In vivo glucose biosensing applications, ECS J. Solid State Sci. Technol. 4 (2015) S3053, https://doi.org/10.1149/2.0141510jss.
[20] S. Metz, M.O. Heuschkel, B. Valencia Avila, R. Holzer, D. Bertrand, Ph. Renaud, Microelectrodes with three-dimensional structures for improved neural interfacing, in: Proc. - IEEE Int. Conf. Eng. Med. Bio. Soc, IEEE, 2001, pp. 765–768, https://doi.org/10.1109/IEMBS.2001.1019053.
[21] M. Dervisevic, E. Dervisevic, L. Esser, C.D. Easton, V.J. Cadarso, N.H. Voelcker, Wearable microneedle array-based sensor for transdermal monitoring of pH levels in interstitial fluid, Biosens. Bioelectron. 222 (2023) 114955, https://doi.org/10.1016/j.bios.2022.114955.
[22] W.-C. Lee, N.G. Gurudatt, D.-S. Park, K.B. Kim, C.S. Choi, Y.-B. Shim, Microneedle array sensor for monitoring glucose in single cell using glucose oxidase-bonded polyterthiophene coated on AuZn oxide layer, Sens. Actuators B Chem. 320 (2020) 128416, https://doi.org/10.1016/j.snb.2020.128416.
[23] S.A.N. Gowers, D.M.E. Freeman, T.M. Rawson, M.L. Rogers, R.C. Wilson, A. H. Holmes, A.E. Cass, D. O'Hare, Development of a minimally invasive microneedle-based sensor for continuous monitoring of β-lactam antibiotic concentrations in Vivo, ACS Sens 4 (2019) 1072–1080, https://doi.org/10.1021/acssensors.9b00288.
[24] T.M. Rawson, S.A.N. Gowers, D.M.E. Freeman, R.C. Wilson, S. Sharma, M. Gilchrist, A. MacGowan, A. Lovering, M. Bayliss, M. Kyriakides, P. Georgiou, A. E.G. Cass, D. O'Hare, A.H. Holmes, Microneedle biosensors for real-time, minimally invasive drug monitoring of phenoxymethylpenicillin: a first-in-human evaluation in healthy volunteers, Lancet Digit. Health 1 (2019) e335–e343, https://doi.org/10.1016/S2589-7500(19)30131-1.
[25] C. Hegarty, A. McConville, R.J. McGlynn, D. Mariotti, J. Davis, Design of composite microneedle sensor systems for the measurement of transdermal pH, Mater. Chem. Phys. 227 (2019) 340–346, https://doi.org/10.1016/j.matchemphys.2019.01.052.
[26] A.T. Satti, J. Park, J. Park, H. Kim, S. Cho, Fabrication of parylene-coated Microneedle array electrode for wearable ECG device, Sensors 20 (2020), https://doi.org/10.3390/s20185183. Article 18.
[27] R. Wang, W. Zhao, W. Wang, Z. Li, A flexible Microneedle electrode array with solid silicon needles, J. Microelectromech. Syst. 21 (2012) 1084–1089, https://doi.org/10.1109/JMEMS.2012.2203790.
[28] C. Robinson, Development of On-Farm Diagnostic Devices, University College Cork, 2020. Doctoral thesis, https://cora.ucc.ie/handle/10468/10886, 2020 (accessed: 30 January 2023).
[29] S.R. Chinnadayyala, S. Cho, Porous platinum black-coated minimally invasive microneedles for non-enzymatic continuous glucose monitoring in interstitial fluid, Nanomaterials 11 (2020) 37, https://doi.org/10.3390/nano11010037.
[30] R. Wang, X. Jiang, W. Wang, Z. Li, A microneedle electrode array on flexible substrate for long-term EEG monitoring, Sens. Actuators B Chem. 244 (2017) 750–758, https://doi.org/10.1016/j.snb.2017.01.052.
[31] A. Bocchino, C. Marquez-Grana, O.P. Singh, E. Melnik, S. Kurzhals, G.C. Mutinati, S. Coulman, C. Martin, K.W. Ng, M. Massufero Vergilio, J. Birchall, P. Donovan, P. Galvin, C. O'Mahony, A multifunctional platform for the production and customization of polymer-based microneedle devices, Sens. Actuators A Phys. 388 (2025) 116491, https://doi.org/10.1016/j.sna.2025.116491.
[32] A. Bocchino, S.R. Teixeira, S. Iadanza, E. Melnik, S. Kurzhals, G.C. Mutinati, C. O'Mahony, Development and characterization of passivation methods for

microneedle-based biosensors, in: Proc. - IEEE Int. Conf. Eng. Med. Bio. Soc, IEEE, 2022, pp. 1275–1278, https://doi.org/10.1109/EMBC48229.2022.9871005.
[33] C. O'Mahony, Structural characterization and in-vivo reliability evaluation of silicon microneedles, Biomed. Microdevices 16 (2014) 333–343, https://doi.org/10.1007/s10544-014-9836-6.
[34] C. O'Mahony, K. Grygoryev, A. Ciarlone, G. Giannoni, A. Kenthao, P. Galvin, Design, fabrication and skin-electrode contact analysis of polymer microneedle-based ECG electrodes, J. Micromech. Microeng. 26 (2016) 084005, https://doi.org/10.1088/0960-1317/26/8/084005.
[35] S.F. Bent, in: A. Nilsson, L.G.M. Pettersson, J.K. Nørskov (Eds.), Chapter 5 - Semiconductor Surface Chemistry, in: Chemical Bonding At Surfaces and Interfaces, Elsevier, Amsterdam, 2008, pp. 323–395, https://doi.org/10.1016/B978-044452837-7.50006-X.
[36] R. Lacerda-Santos, A.B.L. Lima, E.S. Da Penha, A. Dos Santos, F.G. Carvalho, M. M. Pithon, A.F.M. Dantas, In vivo biocompatibility of silicon dioxide nanofilm used as antimicrobial agent on acrylic surface, An. Acad. Bras. Ciênc. 92 (2020) e20181120, https://doi.org/10.1590/0001-3765202020181120.
[37] A. Fernández, A. Redondo, J. Martín-de-León, D. Cantero, PMMA stability under hydrothermal conditions, J. Supercrit. Fluids 198 (2023) 105938, https://doi.org/10.1016/j.supflu.2023.105938.
[38] Y. Minami, T. Tsuyuki, H. Ishikawa, Y. Shimoyama, K. Sato, M. Yoshida, Degradation of stable thermosetting epoxy resins mediated by bases in amide solvents, Polym. J. 57 (2025) 149–162, https://doi.org/10.1038/s41428-024-00979-6.
[39] M.A. Surmeneva, A. Vladescu, C.M. Cotrut, A.I. Tyurin, T.S. Pirozhkova, I. A. Shuvarin, B. Elkin, C. Oehr, R.A. Surmenev, Effect of parylene C coating on the antibiocorrosive and mechanical properties of different magnesium alloys, Appl. Surf. Sci. 427 (2018) 617–627, https://doi.org/10.1016/j.apsusc.2017.08.066.
[40] M. Cieślik, K. Engvall, J. Pan, A. Kotarba, Silane–parylene coating for improving corrosion resistance of stainless steel 316L implant material, Corros. Sci. 53 (2011) 296–301, https://doi.org/10.1016/j.corsci.2010.09.034.
[41] B. He, Y. Yang, M.F. Yuen, X.F. Chen, C.S. Lee, W.J. Zhang, Vertical nanostructure arrays by plasma etching for applications in biology, energy, and electronics, Nano Today 8 (2013) 265–289, https://doi.org/10.1016/j.nantod.2013.04.008.
[42] K.-H. Dahmen, Chemical vapor deposition, in: R.A. Meyers (Ed.), Encyclopedia of Physical Science and Technology, 3rd Edition, Academic Press, New York, 2003, pp. 787–808, https://doi.org/10.1016/B0-12-227410-5/00102-2.
[43] C.A. Schneider, W.S. Rasband, K.W. Eliceiri, NIH image to ImageJ: 25 years of image analysis, Nat. Methods 9 (2012) 671–675, https://doi.org/10.1038/nmeth.2089.
[44] R.K. Kummamuru, L. Hu, L. Cook, M.Y. Efremov, E.A. Olson, L.H. Allen, A close proximity self-aligned shadow mask for sputter deposition onto a membrane or cavity, J. Micromech. Microeng. 18 (2008) 095027, https://doi.org/10.1088/0960-1317/18/9/095027.
[45] Y. Xie, T. Liu, Z. Chu, W. Jin, Recent advances in electrochemical enzymatic biosensors based on regular nanostructured materials, J. Electroanal. Chem. 893 (2021) 115328, https://doi.org/10.1016/j.jelechem.2021.115328.
[46] X. Liu, B. Yin, C. Yang, S. Wu, Passivation strategies for enhancing sensitivity and repeatability of microelectrode electrochemical sensors, Talanta 273 (2024) 125946, https://doi.org/10.1016/j.talanta.2024.125946.
[47] J. Wang, Study of electrode reactions and interfacial properties, John Wiley & Sons. Analytical Electrochemistry, John Wiley & Sons Inc., Hoboken, 2006, pp. 29–66, https://doi.org/10.1002/0471790303.ch2.
[48] Managing blooming in an adhesives process, What's New in Electronics. https://www.wnie.online/managing-blooming-in-an-adhesives-process-2/, 2020 (accessed 21 June 2024).
[49] X. Yan, J. Tang, D. Tanner, J. Ulstrup, X. Xiao, Direct electrochemical enzyme electron transfer on electrodes modified by self-assembled molecular monolayers, Catalysts 10 (2020), https://doi.org/10.3390/catal10121458. Article 12.
[50] P.M. Tsimbouri, L.E. McNamara, E.V. Alakpa, M.J. Daldy, L.-A. Turner, Chapter 7 - cell-material interactions, in: C.A. Van Blitterswijk, J. De Boer (Eds.), Tissue Engineering, 2nd Edition, Academic Press, Cambridge, 2014, pp. 323–395, https://doi.org/10.1016/B978-0-12-420145-3.00007-9.
[51] E. Heydari-Bafrooei, A.A. Ensafi, Nanomaterials-based biosensing strategies for biomarkers diagnosis, a review, Biosens. Bioelectron. X 13 (2023) 100245, https://doi.org/10.1016/j.biosx.2022.100245.
[52] J.Y. Lichtenberg, Y. Ling, S. Kim, Non-specific adsorption reduction methods in biosensing, Sensors 19 (2019), https://doi.org/10.3390/s19112488. Article 11.